Inversion for anisotropy from non-double-couple mechanisms of micro-earthquakes induced during the 2000 injection experiment at the KTB site, Germany

Václav Vavryčuk,[1] Marco Bohnhoff,[2] Zuzana Jechumtálová, [1] Petr Kolář, [1] Jan Šílený[1]

[1] Geophysical Institute, Academy of Sciences of the Czech Republic, Boční II/1401, Praha 4, 141 31, Czech Republic

[2] GeoForschungsZentrum Potsdam, Telegrafenberg, D-14473, Potsdam, Germany

Abstract

A family of 37 most reliable moment tensors of microearthquakes that occurred at a depth level of 5.4 km, having been induced during the 2000 injection experiment at the KTB deep drilling borehole, contain significant non-double-couple (non-DC) components. The DC is on average 60% and the non-DC is 40%. Fault plane solutions computed from the DC part show preferred strike-slip mechanisms with small normal or reverse components. A predominant azimuth of P and T axes is in the range of N140º-160ºE and of N50º-70ºE, respectively. The optimum principal stress directions, inferred from the focal mechanisms, are (azimuth/plunge): $\sigma_1 = 335°/15°$, $\sigma_2 = 110°/70°$, $\sigma_3 = 240°/15°$ and the shape ratio is 0.55. The errors in the plunge and azimuth are about 10º. The non-DC components contain both the isotropic (ISO) and compensated linear dipole (CLVD) components. The mean value of ISO is 1.5%, the mean value of CLVD is -5.7%. The predominantly negative CLVD components are inconsistent with the concept of the non-DC mechanisms as a result of tensile faulting due to fluid injection into the rock. The non-DC components have probably three other major origins: random numerical errors produced by the moment tensor inversion due to noise and limitations of input data, systematic errors produced by mismodeling of the medium when calculating the Green functions, and anisotropy in the focal area. Anisotropy is a very likely origin of non-DC components, because a rather

strong seismic anisotropy has been observed at the KTB site with strength up to 20% for P waves, and attributed to foliated crystalline rocks composed of gneiss and amphibolite. Adopting four alternative models of anisotropy obtained by other seismic measurements at the KTB, we have employed the non-DC components for estimating an optimum orientation of anisotropy in the focal area. The optimum orientation of the symmetry plane of anisotropy is nearly vertical with a strike of N335-340ºE. This strike coincides well with the strike of 330º typical for many major lithological units and faults and with the orientation of the transversely isotropic model inferred by other authors. A successful inversion for anisotropy orientation confirms that a significant part of the non-DC components of the moment tensors under study is produced by anisotropy, and that the moment tensors can be used to estimate the anisotropy.

1. Introduction

A 60-day long-term fluid injection experiment was performed at the German KTB superdeep drilling hole in 2000 (Baisch et. al. 2002). The KTB site is located in southeast Germany at the western margin of the Bohemian Massif and the contact zone of the Saxothuringian with the Moldanubian (Wagner et al. 1997). About 4000 m^3 of water were injected into the well head to induce seismicity near the open-hole section at a depth of 9.1 km. The entire borehole was pressurized and the well head pressure gradually increased during the experiment from 20 to 30 MPa. The injection was interrupted by several sharp pressure drops during shut-in phases. The injected fluid induced seismicity not only at the target depth but also at shallower depths because of leaks in the borehole casing. The seismicity was monitored by a surface network of 40 three-component seismic stations and by one downhole three-component sensor at a depth of 3.8 km, situated at the nearby pilot hole. A total of 2799 induced microearthquakes were detected at the downhole sensor, and 237 of them were located having good signal-to-noise ratios at the surface stations (Baisch et. al. 2002). The event locations revealed that the hypocenter distribution is complex and displays strong spatial and temporal clustering. Fault plane solutions have been calculated for 125 strongest events with the best signal-to-noise ratio (Bohnhoff et al. 2004). The fault plane solutions show preferred strike-slip mechanisms with a predominant azimuth in the

range of N160°-180°E for P axes and of N50°-80°E for T axes. The mechanisms are in good agreement with the stress field at the KTB (Brudy et al. 1997) and in western and central Europe (Müller et al. 1992).

In this paper, we continue studying the seismicity induced during the 2000 injection experiment and try to estimate moment tensors of selected events. Evaluating the complete moment tensors we can get more detailed information on the geometry of fractures, the fracture process and on the properties of fractured rock (Sipkin 1986; Frohlich 1994; Julian et al. 1997, 1998; Miller et a. 1998). A careful evaluation of the moment tensors and their DC and non-DC components of events induced during the injection can address several intriguing topics not yet well understood, such as the role of the injected fluid on the type of faulting and the effects of anisotropy in the focal area on focal mechanisms.

It is known that high pore pressure associated with an injection destabilizes fractures and triggers microearthquakes. If pore pressure is sufficiently high, it can even cause hydraulic fracturing or opening of existing faults (Vavryčuk 2002). Since the elevated pore fluid pressure remained below the least principal value of the background stress during the KTB injection experiment in 2000 (Baisch & Harjes, 2003), hydraulic opening of existing fractures was seen to be unlikely. Consequently, predominantly shear events with no tensile component should be observed. However, inhomogeneities and the presence of the hole in the medium could affect the background stress and cause its perturbations. This would invalidate the above assumption and lead to the occurrence of combined shear and tensile faulting. Since moment tensors are very sensitive to the presence of a tensile component in faulting, they can be used to vindicate it. Vavryčuk (2001) showed that even small deviations from shear faulting can be detected by evaluating the moment tensors. For example, a 10° declination of slip from the fault results in lowering the percentage of the DC component in the moment tensors from 100% to 70%, and a 20° declination causes a drop of the DC from 100% to a mere 50% (Vavryčuk 2001). Such drops of the DC component in moment tensors should be easily detected in well-determined moment tensors.

In evaluating moment tensors we can also address the question: How significant is anisotropy in the focal area? Vavryčuk (2005, 2006b) has shown that moment tensors are affected by anisotropy of the rock surrounding the fault. While shear faulting on planar faults in an isotropic medium produces a pure DC mechanism, shear faulting on planar

faults in an anisotropic medium produces a general mechanism with DC as well as non-DC components. Shear faulting in anisotropic rocks present in the Earth's crust can produce moment tensors with non-DC components up to 40-50%. This percentage depends on the strength and symmetry of anisotropy and on the orientation of faulting. If we evaluate a set of accurate moment tensors of events that occurred in a homogeneous anisotropic focal area on differently oriented faults, we can invert them for anisotropy (Vavryčuk 2004, 2006a).

2. Data

We analyzed 55 microearthquakes with foci at depth level of 5.4 km. At this level, 80% of the seismic events occurred during the injection experiment (see Baisch & Harjes, 2003, Fig. 2). The events under study form a subset of events previously analyzed by Bohnhoff et al. (2004). The events were recorded at least at 5 surface stations while most of them were recorded at 20 or more surface stations (see Tab. 1). The stations were equipped with PDAS-100 data logger and with three-component seismometers Mark L4-3c. The recording was continuous at a 200 Hz sampling rate. The recorded velocigrams were filtered by a bandpass Butterworth filter of 4^{th} extracting signal frequencies between 2.5 Hz and 40 Hz with enhanced signal-to-noise ratio. The velocigrams were further integrated to obtain displacement records. From these records, particle motions of P and S waves were plotted and the first maximum P- and S-wave amplitudes were interactively picked.

3. Moment tensor inversion

The amplitude ratios of SH/P, SV/P and SV/SH were computed from the P and S amplitudes picked from particle motions. These ratios together with the polarities of P waves were inverted for complete moment tensors (Jechumtálová & Šílený, 2005). The model of the medium and event locations, required to compute the synthetic amplitude ratios were adopted from Baisch et al. (2002). The cost function was constructed as the sum of differences of the logarithms of the observed and synthetic amplitude ratios. The logarithms of amplitude ratios were used because they appeared to be more stable than if

simple ratios were used. No constraint on the moment tensors (e.g., the zero-trace condition) was imposed in the inversion, hence the inversion was able to yield the full moment tensors with unconstrained DC and non-DC components. Although the inversion from amplitude ratios is nonlinear and more complex than from amplitudes, it is less vulnerable to erroneous modeling of the Earth's crust and to inaccuracies in the calibration of instruments. Since the inversion is based on amplitude ratios and P-wave polarities, it yields relative but not absolute values of the moment tensors.

The stability of the moment tensors retrieved was tested by observing the distributions of 100 solutions obtained by inverting the data contaminated by artificial random noise with the maximum amplitude reaching 5% of the top value in each channel. In this way, the distribution of the principal axes of moment tensors was obtained providing information on the stability of the orientation of their deviatoric part, i.e. the orientation of the DC and CLVD components. In addition, the bundles of nodal lines are plotted to display the stability of the fault plane solution. As an example of a reliably determined DC mechanism, event 252.199 is presented in Fig. 1: the principal axes of the moment tensors from the multiple processing of noisy data are close together, which indicates that the orientation of the mechanism is well constrained. The reliability of the solution is manifested also by the tight clustering of nodal lines. Figure 2 shows event 259.065 as an example of an unreliably determined mechanism. The orientation of the mechanism is poorly determined: the principal axes are scattered widely, and the zones of T and N axes are mixed together.

In analyzing the stability of the 55 inverted moment tensors, we selected 37 of the most reliable moment tensors for the purpose of our study (see Tab. 1). These moment tensors displayed well-defined clustering of nodal lines in multiple inversions of data contaminated by noise, and the clusters of P, N and T axes were isolated and did not overlap. Moreover, the sum of standard deviations of the DC, ISO and CLVD components was constrained to be less than 50% (see Tab. 2).

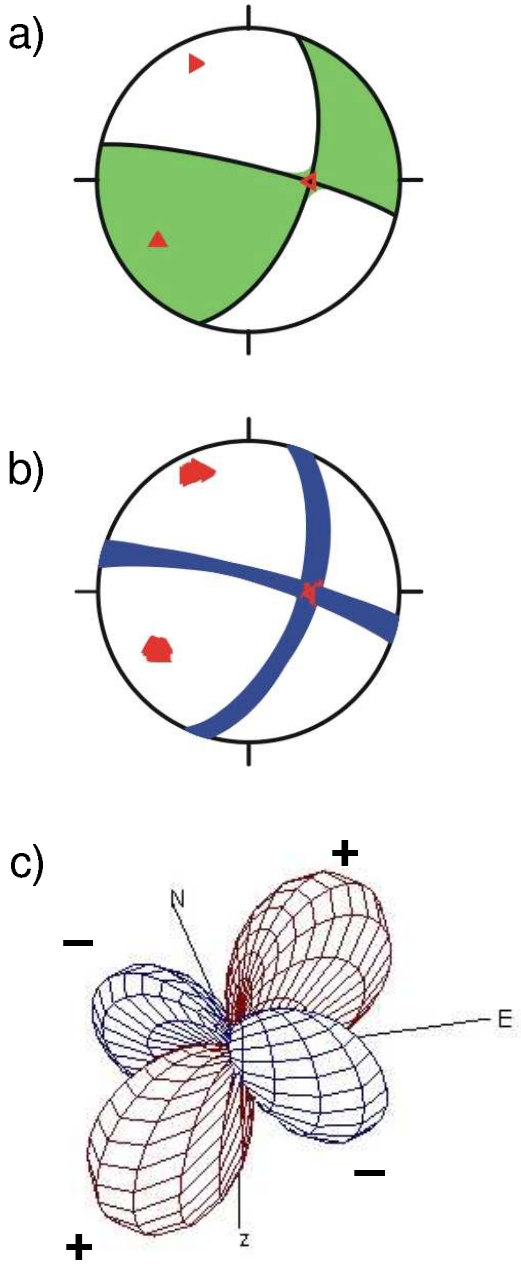

Figure 1. An example of a reliably determined mechanism (event 252.199 in Tab. 1). The figure shows: (a) the optimum fault-plane solution (the nodal lines of the DC part), (b) the distribution of the P, N and T axes and of nodal lines obtained by the inversion of noisy data, and (c) the P-wave radiation function. The green area in plot (a) marks the zone of compressions corresponding to the complete moment tensor. The moment tensor principal axes are marked by triangles: pointing up – tensional (T) axis, pointing left – null (N) axis, pointing right – pressure (P) axis. Clustering of P, N and T axes and of nodal lines in plot (b) testifies the stability of the solution. E, N and Z in plot (c) denote North, East and the vertical axis. The plus and minus signs define the polarity of the P wave.

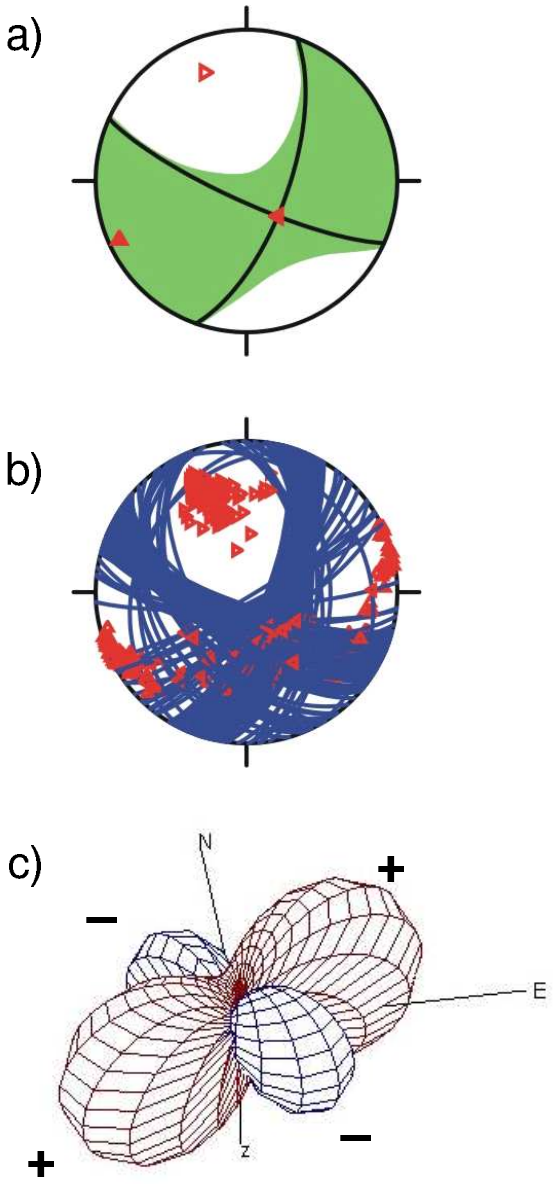

Figure 2. An example of an unreliably determined mechanism. For details, see the caption of Fig.1.

Table 1. Locations and moment tensors

No.	Event identification	*Mw*	N^S	N [m]	E [m]	Z [m]	M_{11}	M_{12}	M_{13}	M_{22}	M_{23}	M_{33}
1	235.008	0,38	21	-90	80	5 310	-0,90	1,54	0,70	1,10	-0,40	0,82
2	235.025	-0,34	11	-80	-150	5 320	-1,00	1,08	-0,34	1,42	-0,04	-0,06
3	236.041	1,10	27	-130	-40	5 340	-1,00	0,68	-0,96	0,64	0,24	-0,24
4	237.024	-0,05	7	-10	30	5 130	-0,34	1,52	-0,94	1,04	0,16	0,20
5	252.199	0,47	30	-90	-10	5 310	-0,88	1,24	-0,84	0,68	-0,42	0,28
6	255.002	-0,11	23	-120	50	5 430	-0,90	1,54	-0,12	0,28	-0,12	-0,02
7	258.009	0,06	5	70	-130	5 410	0,26	1,52	-0,72	1,30	0,18	0,48
8	258.010	0,07	13	-110	-100	5 330	-0,88	1,04	-0,90	0,46	1,02	0,40
9	259.065	0,22	9	-120	-40	5 270	1,10	1,54	-0,66	1,32	0,04	0,20
10	261.016	0,02	13	-120	-30	5 340	-0,78	1,26	-0,32	0,90	-0,02	0,06
11	262.070	-0,55	32	-100	-40	5 370	-0,96	1,52	-0,80	0,18	-0,38	0,44
12	264.012	-0,69	9	-100	-40	5 300	1,32	1,46	-0,88	1,42	0,24	0,14
13	264.084	-0,01	7	-100	-100	5 370	-0,80	1,00	0,26	-0,20	0,12	-0,96
14	266.058	0,55	31	10	-100	5 340	-0,84	1,34	-0,46	1,06	0,52	-0,22
15	267.134	0,14	20	220	10	5 330	-0,42	0,82	-0,38	1,44	0,14	-0,50
16	268.172	0,18	25	-10	-90	5 450	1,20	0,70	1,08	1,32	0,42	-0,72
17	269.055	-0,01	20	-50	-70	5 330	-0,90	1,46	-0,76	1,48	0,20	-0,22
18	271.280	0,15	29	-360	170	5 200	-1,00	1,08	-0,42	0,64	0,66	0,02
19	275.016	0,92	31	-100	40	5 370	-0,96	1,48	-0,80	0,92	0,52	-0,40
20	275.026	0,21	21	-40	20	5 340	-1,00	1,18	-0,56	0,22	-0,90	0,02
21	275.027	0,87	33	-160	20	5 330	-0,98	1,54	-0,72	0,08	-0,08	0,30
22	275.094	-0,13	18	-290	0	5 470	-1,00	1,22	0,46	-0,78	0,08	0,06
23	276.086	0,05	13	-60	-150	5 290	1,06	1,30	1,22	1,38	-0,50	0,04
24	278.066	0,06	9	-110	60	5 480	-0,64	1,52	1,36	0,32	-0,16	0,38
25	279.073	0,17	21	-10	-40	5 350	-0,86	1,08	-1,00	1,12	-0,94	0,30
26	279.110	-0,19	13	120	-120	5 200	0,20	1,40	-0,66	-1,00	-0,72	-0,02
27	280.054	0,35	20	-220	40	5 350	-0,04	1,34	-0,32	-0,22	-0,10	-0,98
28	281.018	0,20	30	-80	-80	5 330	-0,94	1,44	-0,66	1,08	0,00	-0,54
29	281.047	0,72	31	-30	-10	5 360	-0,72	1,52	-0,66	0,74	-0,26	0,10
30	282.012	-0,05	17	-90	10	5 360	-0,22	1,54	-0,44	0,74	-0,16	-0,18
31	283.005	-0,13	8	0	-330	5 200	0,16	1,48	0,70	1,02	0,14	-0,56
32	285.056	-0,26	16	-270	50	5 580	-0,98	-0,14	-0,78	1,40	-0,72	-0,04
33	286.001	0,23	20	-170	160	5 210	-1,00	1,20	-0,34	1,50	-0,14	0,36
34	288.030	-0,11	21	-230	50	5 570	-0,92	1,32	-0,26	-0,92	-0,92	0,24
35	290.048	1,02	28	-140	-10	5 300	-0,98	1,46	-0,64	0,44	0,90	0,38
36	291.059	-0,07	11	-150	170	5 250	-0,86	1,10	-0,98	1,46	-0,06	0,76
37	297.016	0,40	10	-150	-200	5 640	-0,94	1,52	0,06	-0,40	-0,08	0,28

Mw is the body wave local magnitude, N^S is the number of surface stations, which detected the event, N, E, Z are coordinates of the hypocenter, and M_{11}, M_{22}, M_{33}, M_{12}, M_{13} and M_{23} are the components of moment tensor **M** in relative values. The locations of events were adopted from Baisch et al. (2002).

Table 2. DC and non-DC components

No.	Strike [°]	Dip [°]	Rake [°]	DC [%]	ISO [%]	CLVD [%]	σ^{DC} [%]	σ^{ISO} [%]	σ^{CLVD} [%]	σ^{SUM} [%]
1	288	78	-169	31,7	17,3	-51,1	10,35	5,15	12,93	28,43
2	115	85	-168	79,6	6,5	13,9	11,03	3,63	9,75	24,41
3	118	74	-151	29,8	-10,8	-59,4	15,03	4,43	11,28	30,74
4	104	82	-153	66,8	14,3	-18,9	11,98	10,75	18,22	40,95
5	284	82	147	97,3	1,5	1,2	7,43	3,76	8,97	20,16
6	280	86	174	71,4	-10,9	-17,7	9,37	3,67	9,21	22,25
7	102	80	-157	67,3	28,0	-4,7	10,53	7,18	17,23	34,94
8	108	38	167	39,0	-0,3	-60,7	19,42	7,80	21,90	49,12
9	97	75	-149	39,3	30,9	29,7	11,53	4,06	14,82	30,41
10	107	87	-168	92,7	3,8	-3,6	6,68	4,50	7,56	18,74
11	276	76	149	79,9	-5,4	-14,7	9,81	6,75	12,28	28,84
12	99	69	-141	54,6	33,0	12,4	11,12	4,08	14,72	29,92
13	279	87	-164	28,7	-41,5	29,9	4,70	6,62	6,49	17,81
14	110	69	-169	98,4	0,0	-1,6	6,94	3,63	7,41	17,98
15	121	65	-152	48,1	9,9	42,0	12,13	4,52	9,47	26,12
16	301	66	-104	68,2	25,7	-6,1	9,91	2,84	10,85	23,60
17	112	76	-160	94,3	5,5	0,2	3,78	2,61	5,50	11,89
18	110	61	-179	66,3	-6,3	-27,4	13,60	5,05	10,79	29,44
19	110	70	-162	73,1	-6,5	-20,4	8,76	3,36	6,54	18,66
20	279	68	155	47,1	-14,7	38,2	11,13	5,05	13,40	29,58
21	276	81	153	55,3	-9,1	-35,6	8,81	3,20	11,27	23,28
22	86	71	148	35,8	-26,6	-37,6	9,00	3,21	10,01	22,22
23	281	70	-137	47,5	31,5	-21,0	10,40	7,74	9,97	28,11
24	94	86	138	57,2	0,9	-41,9	18,47	10,30	20,52	49,29
25	291	83	140	53,2	7,8	39,0	10,71	4,24	8,69	23,64
26	254	63	164	63,7	-14,0	22,3	9,19	5,04	12,38	26,61
27	90	84	-163	23,4	-27,3	49,3	13,12	6,74	14,26	34,12
28	110	79	-158	74,8	-6,9	18,3	6,41	3,41	10,62	20,44
29	282	87	157	94,8	2,1	3,1	10,65	5,27	11,92	27,84
30	99	89	-164	62,5	5,8	31,7	13,53	4,90	10,85	29,28
31	285	74	-145	43,8	9,2	47,0	18,53	6,29	15,25	40,07
32	140	85	-139	87,3	7,4	-5,3	4,40	1,72	4,81	10,93
33	293	89	168	79,1	14,2	-6,7	9,01	2,38	10,20	21,59
34	262	52	154	70,3	-22,9	-6,8	5,22	11,66	16,28	33,16
35	105	56	177	43,0	-2,3	-54,6	9,62	3,97	9,50	23,09
36	292	90	150	42,2	22,0	-35,8	14,31	5,54	12,27	32,12
37	275	87	-180	26,7	-15,9	-57,4	17,34	8,22	18,77	44,33
Mean	---	---	---	60.4	1,51	-5,70	10,65	5,22	11,81	27,68

The percentages of the DC, ISO, and CLVD were computed using eqs (15-17) of Vavryčuk (2005). The quantities σ^{DC}, σ^{ISO}, and σ^{CLVD} are the standard deviations of the DC, ISO and CLVD percentages, σ^{SUM} is defined as $\sigma^{SUM} = \sigma^{DC} + \sigma^{ISO} + \sigma^{CLVD}$.

4. Focal mechanisms and tectonic stress

The fault plane solutions of the 37 selected events with the most reliable moment tensors are listed in Tab. 2 and shown in Fig. 3a. In accordance with Bohnhoff et al. (2004), the fault plane solutions show preferred strike-slip mechanisms with small normal or reverse components. The P and T axes are well clustered (see Fig. 3b) having a predominant azimuth in the range of N140°-160°E and N50°-70°E, respectively.

The focal mechanisms were inverted for tectonic stress by applying the Gephart & Forsyth inversion method (Gephart & Forsyth 1984; Gephart 1990; Michael 1987; Lund & Slunga 1999). This method assumes that (1) the stress is uniform in the region, (2) the earthquakes occur on existing faults with varying orientations, and (3) the slip vector points in the direction of the resolved shear traction on the fault. The stress tensor is sought by minimizing the sum of deviations between the shear traction directions and the observed slips at the faults. The misfit function is minimized by using the grid search inversion scheme. The maximum compression σ_1 is normalized to be -1, and the trace of the stress tensor is assumed to be zero, $\sigma_1 + \sigma_2 + \sigma_3 = 0$. The inversion yields three angles defining the directions of the three principal stress axes, and shape ratio R, $R = (\sigma_1 - \sigma_2)/(\sigma_1 - \sigma_3)$.

The inversion for the optimum stress was performed using a 5° grid in seeking the principal stress directions, and a 0.01 increment in seeking σ_2. The optimum principal stress directions are (azimuth/plunge): $\sigma_1 = 335°/15°$, $\sigma_2 = 110°/70°$, $\sigma_3 = 240°/15°$ and the shape ratio is 0.55 (Fig. 4). The errors in the plunge and azimuth are estimated to be about 10°. The average deviation angle between the predicted shear tractions and observed slips is 6.0°.

The resolved stress is consistent with the results of Müller et al. (1992), Plenefisch and Bonjer (1997) and Brudy et al. (1997) obtained for western and central Europe from various types of data, for northern Rhine Graben from focal mechanisms, and for the KTB site from breakouts, respectively (see Fig. 5, Tab. 3). The stress orientation at the KTB has been estimated using focal mechanisms also by Bohnhoff et al (2004), who obtained stress directions rotated by about 20° clockwise compared to our results. This bias might be scaling-related as we considered only the 37 largest events whereas Bohnhoff et al. (2004) discuss scaling-related changes in stress field heterogeneity based on 125 focal

mechanisms. Interestingly, there is no big discrepancy in distribution of P and T axes for the larger events that show a strongly preferred orientation whereas the weaker events partly deviate from that orientation (our Figure 3, their Figure 11). However, we need to consider that their mechanisms were calculated using the FOCMEC program (Snoke 2003), which is designed just for retrieving pure DC mechanisms, and thus the non-DC components in the moment tensors as discussed further below might be responsible for the discrepancies in deduced stress field orientation. Besides, also the different level of similar focal mechanisms inverted for the stress tensor might play a role for the results obtained.

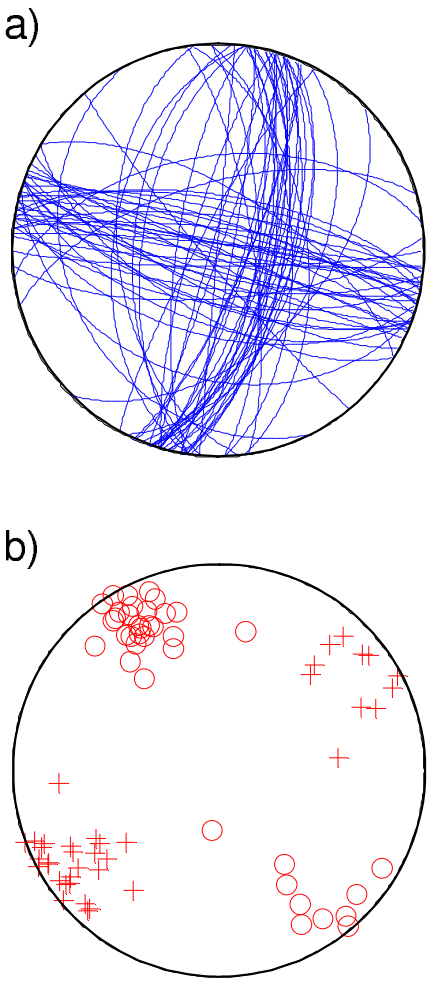

Figure 3. Focal mechanisms of 37 events under study. (a) nodal lines, (b) P(o)/T(+) axes. Lower-hemisphere equal-area projection is used.

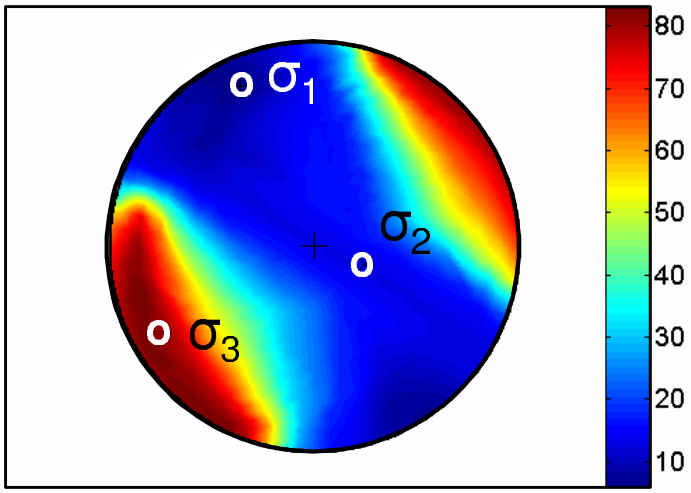

Figure 4. Inversion for stress. The plot shows the misfit function for stress axis σ_1. The misfit function is defined as the average deviation (in degrees) of the predicted shear traction directions from the observed slips at the faults. Lower-hemisphere equal-area projection is used. The optimum directions of the principal stresses are marked by circles.

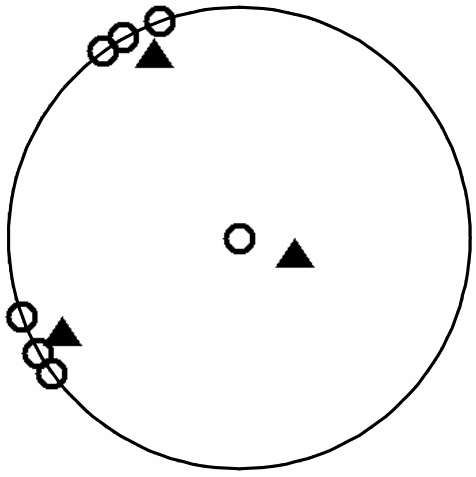

Figure 5. A comparison of principal stress directions obtained in this paper (full triangles) with those published by other authors (open circles). For values of stress directions and for references, see Tab. 3.

Table 3. Stress axes and shape ratio at the KTB site and in the adjacent areas.

Reference	Site	σ_1 (azimuth/plunge)	σ_2 (azimuth/plunge)	σ_3 (azimuth/plunge)	R
This paper	KTB	335°/15°	110°/70°	240°/15°	0.55
Brudy *et al.* (1997)	KTB	340°/0°	Vertical	250°/0°	0.72
Plenefisch & Bonjer (1997)	Rhine Graben	330°/0°	Vertical	240°/0°	0.5
Müller *et al.* (1992)	Western Europe	324°/0°	Vertical	234°/0°	---

The azimuth is measured clockwise from North; the plunge is measured downwards from the horizontal direction.

5. Non-DC components

5.1. Amount of the non-DC components in the moment tensors

The retrieved moment tensors contain significant non-DC components (see Tab. 2). The DC is on average 60% and the non-DC is 40%. The non-DC components contain both the isotropic component (ISO) and the compensated linear vector component (CLVD), which take positive as well as negative values. Figure 6 shows an example of an event with positive ISO and CLVD, Fig. 7 shows an event with negative ISO and CLVD. The radiation functions of both events remarkably deviate from the standard quatrefoil form known for DC mechanisms. On average, the CLVD is more pronounced than the ISO: the mean absolute value is 26.1% for the CLVD, but only 13.5% for the ISO. Also the distribution of the CLVD values is different from that of ISO (see Fig. 8). While the distribution of the ISO values is nearly symmetric with a mean value of 1.5%, the CLVD values tend to be more negative, and the mean value is -5.7%. Hence, the compressive components slightly prevail over tensile components.

5.2. Possible causes of the non-DC components

The non-DC components may be of several possible origins:

(1) They can be spurious being an artefact of an inaccurate moment tensor inversion due to data limitations and erroneous location of the source. To estimate the errors of the moment tensor inversion, we tested its stability and sensitivity to noise in the data and

evaluated the standard deviations of the results (see Tab. 2). The mean standard deviations of the DC and non-DC components are estimated to be 10.7% for the DC, 11.8% for the CLVD, and 5.2% for ISO. Although these values are high, it is clear that the presence of the non-DC components cannot be fully explained by the inaccuracy of the moment tensor inversion.

(2) The non-DC components may originate in shear faulting on a non–planar fault or on a fault composed of several differently oriented subfaults (Sipkin 1986; Frohlich 1994). Such mechanisms, however, can never contain an ISO component, because no combination of DC moment tensors, produced by individual sub-events, can generate a non-zero ISO (Julian et al. 1998). Since the ISO is significant in the studied dataset, and it is not reasonable to assume that the majority of microearthquakes displayed a complicated faulting geometry, we conclude that this origin is not responsible for the majority of retrieved non-DC components.

(3) The non-DC components may be produced by tensile faulting owing to high pore pressure. Pore pressure can decrease effective stress on faults and trigger earthquakes. If pore pressure is sufficiently high, it can open the fault during an earthquake and the resultant mechanism is a combination of shear and tensile faulting (Shimizu et al. 1988; Ross et al. 1996; Julian et al. 1998; Miller et al. 1998, Vavryčuk 2001, 2002). Such mechanisms should contain both CLVD and ISO components, which must be positive, and their ratio depends on the Poisson ratio at the source (Vavryčuk 2001). Since the microearthquakes studied are induced by fluid injections into the rock, pore pressure might be anomalous, and the possibility of tensile faulting cannot be excluded. However, the negative mean value of the CLVD and the nearly zero mean value of the ISO indicate that tensile faulting cannot be the predominant origin of the non-DC components in the studied dataset.

(4) One of possible origins of the non-DC components is seismic anisotropy. Anisotropy can produce non-DC mechanisms in two ways. Firstly, if anisotropy is neglected and isotropic Green functions are used in the moment tensor inversion, the inversion yields spurious non-DC components (Šílený & Vavryčuk 2000, 2002). Secondly, shear faulting in anisotropic focal area produces generally non-DC mechanisms (Kawasaki & Tanimoto 1981; Rössler et al. 2004; Vavryčuk 2005, 2006b). The non-DC components depend on symmetry and strength of anisotropy, and on the orientation of faulting with

respect to the anisotropy axes. Hence, even in the case of using correct anisotropic Green functions in the moment tensor inversion, we should obtain non-DC components, which are true and physical. The non-DC components can comprise both the ISO and CLVD and can attain positive as well as negative values. Since several studies confirmed that the rocks in the KTB environment are anisotropic (Rabbel 1994; Jahns et al. 1996, Okaya et al. 2004; Rabbel et al. 2004) it is very likely that anisotropy is responsible at least for a part of the non-DC components.

6. Anisotropy in the focal area

In this section we shall examine the possibility of the non-DC components in moment tensors being produced by anisotropy in the focal area. We shall provide a theoretical background explaining how anisotropy can affect moment tensors and describe a method of determining anisotropy parameters from their non-DC components. Finally, we shall try to extract some information on anisotropy in the focal area from the observed data.

6.1. Moment tensors in anisotropic media

The seismic moment tensor **M** in anisotropic media is expressed as (Vavryčuk 2005, eq. 4)

$$M_{ij} = c_{ijkl} D_{kl}, \tag{1}$$

where c_{ijkl} are the elastic parameters of the medium, and D_{kl} is the source tensor defined as

$$D_{kl} = \frac{uS}{2}\left(\nu_k n_l + \nu_l n_k\right). \tag{2}$$

Vectors **v** and **n** specify the fault normal and slip direction, u is the slip and S is the fault area. If the slip vector lies in the fault plane, the earthquake is shear, if the slip vector is inclined from the fault plane, the earthquake is non-shear (tensile or compressive, see Vavryčuk 2001).

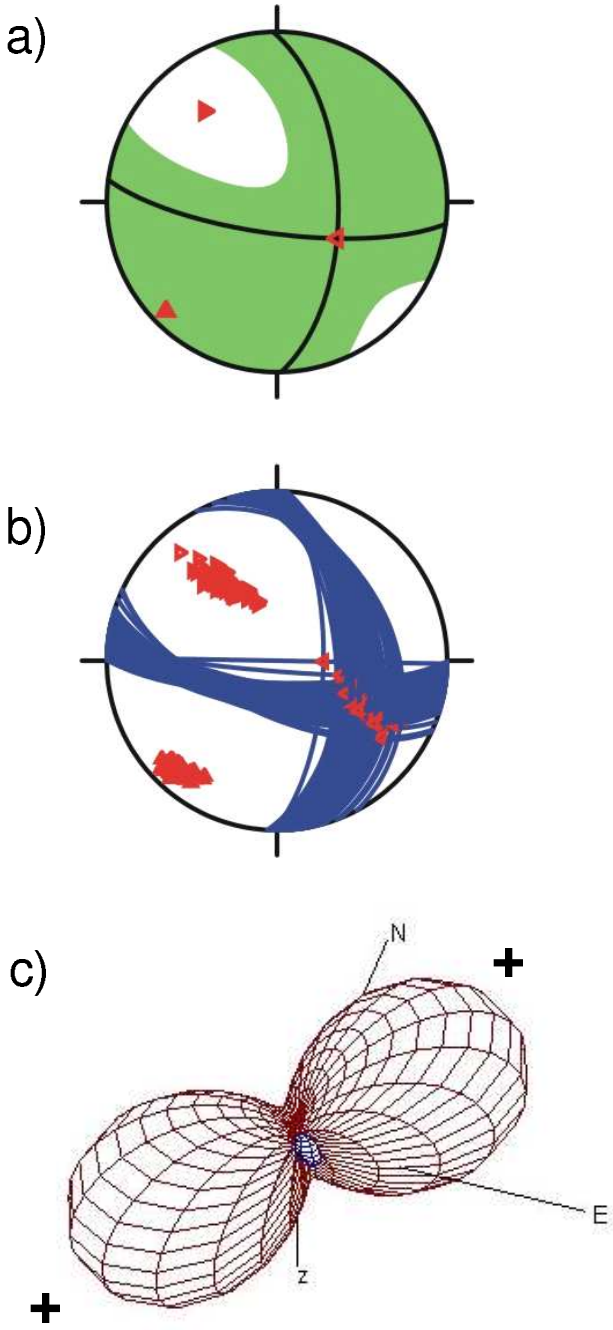

Figure 6. An example of an extensive mechanism with positive ISO and CLVD components (event 259.065 in Tab. 1). For details, see the caption of Fig.1.

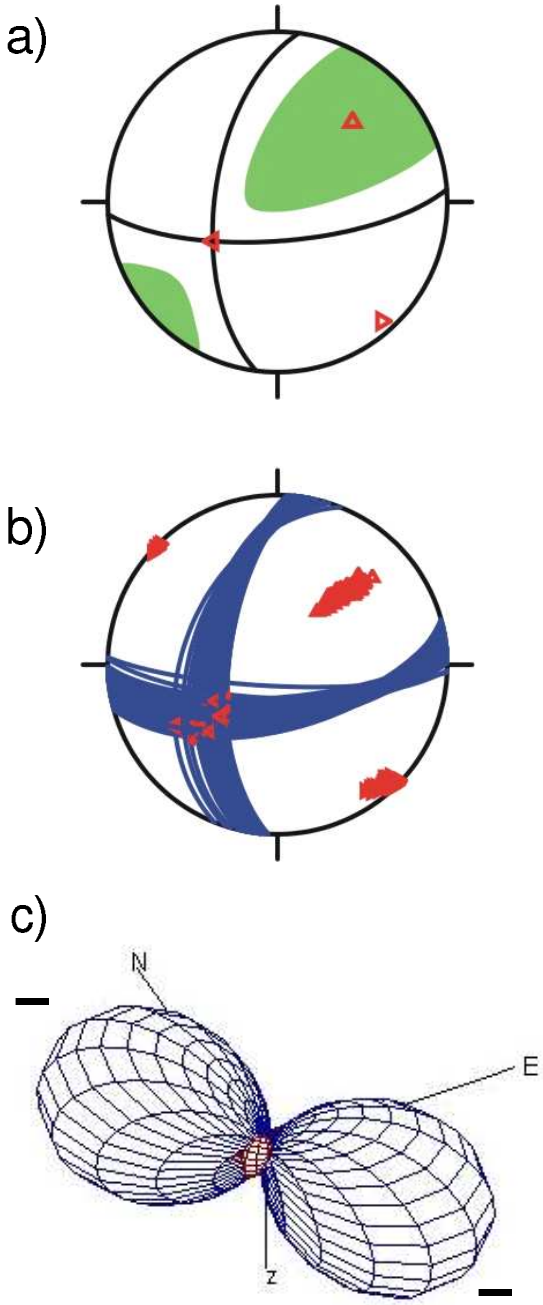

Figure 7. An example of a compressive mechanism with negative ISO and CLVD components (event 275.094 in Tab. 1). For details, see the caption of Fig.1.

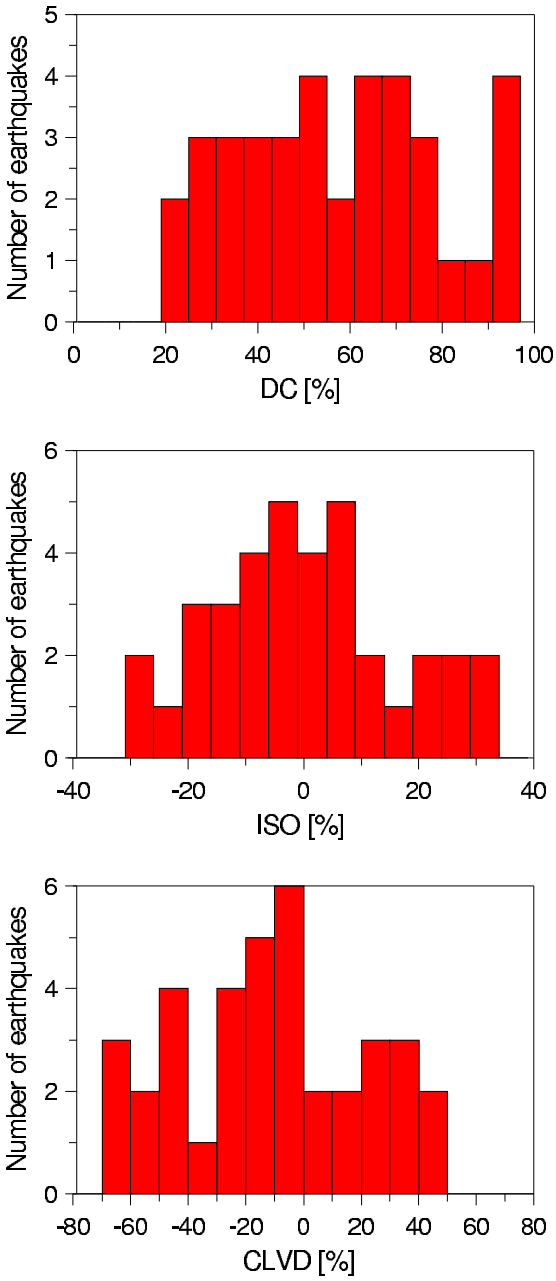

Figure 8. Histograms of the percentages of the DC and non-DC components. The percentages of the DC, ISO, and CLVD were computed using eqs (15-17) of Vavryčuk (2005).

Since source tensor **D** is formed by a dyad of vectors **v** and **n**, it should always have one zero eigenvalue, and subsequently its determinant must be zero:

$$\mathrm{Det}(\mathbf{D}) = 0\,. \tag{3}$$

If faulting is shear, tensor **D** is constrained to have also zero trace:

$$\mathrm{Trace}(\mathbf{D}) = uS\,(\mathbf{n}\cdot\mathbf{v}) = 0\,, \tag{4}$$

Equations (3) and (4) can be used to an advantage in defining the misfit function in the inversion for anisotropy. If we know the moment tensors of many earthquakes that occurred in at the same source area, we can invert for elastic parameters c_{ijkl} minimizing the sum of absolute values of Det(**D**) for all earthquakes. If we are confident that the studied earthquakes are shear, we can minimize the sum of absolute values of Det(**D**) and Trace(**D**) for all earthquakes. The method can be modified to be applicable also to the inversion from moment tensors, which are constrained to have zero trace (see Vavryčuk 2004). As expected, if we invert DC moment tensors, the procedure yields an isotropic medium; if we invert the non-DC mechanisms, we can obtain anisotropy.

6.2. Inversion algorithm

The extent and quality of a moment tensor data set limit the number of anisotropic parameters which can be inverted for. A general triclinic anisotropy is defined by 21 elastic parameters. However, one of them must always be fixed because of coupling of elastic parameters c_{ijkl}, slip u and fault area S. If we invert from moment tensors of shear earthquakes, another elastic parameter must be fixed because of a special geometry in shear faulting (Vavryčuk 2004). Hence, one can invert at the most for 20 elastic parameters when using moment tensors of non-shear earthquakes, or for 19 parameters when using moment tensors of shear earthquakes. This requires at least data of 20 non-shear earthquakes, on which we impose condition (3). Each non-shear earthquake thus represents one equation for the anisotropy parameters. If we invert data of shear earthquakes, we need at least 10 moment tensors, on which we impose conditions (3) and (4). In this case, each earthquake represents two equations for the anisotropy parameters. However, because of noise in the

data, it is more plausible to invert for anisotropy of higher symmetry to reduce the number of unknowns and to use a much larger number of moment tensors.

Synthetic tests show that an optimum number of accurately determined moment tensors is about 100 when inverting for orthorhombic anisotropy of arbitrary orientation. The moment tensors of non-shear earthquakes can be used, and the misfit function is constructed as the sum of the absolute values of Det(**D**). Since the number of moment tensors under study is rather small and their accuracy is limited, the inversion for both the elastic parameters and the anisotropy orientation is not possible. Therefore, we must reduce the number of unknowns to stabilize the inversion. This can be done by fixing the elastic parameters and focusing just on finding the optimum orientation of anisotropy. Restricting the inversion to finding only the orientation of anisotropy reduces the number of unknowns either to 3 angles, defining the axes of orthorhombic anisotropy or of anisotropy of lower symmetry, or to 2 angles, defining the symmetry axis of transverse isotropy. Obviously, the restricted inversion can work, provided we know the symmetry of anisotropy and have reasonable estimates of anisotropy in the focal area evaluated in the coordinate system of the anisotropy axes.

6.3. Anisotropy at the KTB site

The site of the KTB deep drilling borehole is characterized by a complex and heterogeneous crystalline crust (Emmermann & Lauterjung 1997). The rock drilled at the KTB basically consists of alternating felsic and mafic layers, mainly biotite gneiss and amphibolite (Rabbel et al. 2004). The layers were steeply folded with dips between 60-90°, with penetrative foliation between 50-80°. Field mapping, regional geophysics, and borehole results indicate that the region can be viewed as a block of steeply dipping foliated rocks with a uniform N330°E strike (Berkhemer et al. 1997; Okaya et al. 2004). In such rocks, preferred orientations of minerals prevail, and the crust may display a significant anisotropy. Anisotropy strength might be as high as 17-20% for P waves, and similar or even higher for S waves (Babuška & Cara 1991).

Seismic anisotropy of rocks at the KTB site has been estimated by various authors, using various methods. Rabbel et al. (2004) published elastic parameters of lithologically identical gneiss units at three different depth intervals of the KTB well: 2.2-3.0 km, 7.6-7.9 km, and 7.9-8.2 km. The elastic parameters describe transverse isotropy and were obtained

by combining the data of VSP and the dip of rock foliation based on formation micro-scanner logs. Jahns et al. (1994, 1996) reported several sets of elastic parameters of the KTB paragneiss determined using VSP, sonic data and laboratory measurements on a rock sample. The models obtained from the VSP and sonic data are transversely isotropic, the laboratory model is orthorhombic having been computed from velocities of P waves using the approach of Klima (1973). Jahns et al (1996) also tried to take into account the effects of in situ water saturation on laboratory measurements, which are usually performed on dry rocks, and proposed two other hypothetical models of the water-saturated KTB paragneiss.

For the purpose of this study, we have employed four anisotropy models, published by Jahns et al. (1996) and Rabbel et al. (2004). The models were obtained from VSP data, sonic logs and from laboratory measurements. Three models are transversely isotropic and one model is orthorhombic (see Tab. 4). The models predict different directional variations of velocities and also different anisotropy strengths. The P-wave anisotropy varies between 2-18%, and the S-wave anisotropy varies between 3-26% (see Tab. 5). Since the models comprise a fairly high variety of anisotropic behavior (see Figs. 9 and 10), we assume that the true anisotropy is within this variety. In the next, we shall invert for an optimum anisotropy orientation, using all four alternative models, and compare the retrieved orientation with that obtained by other methods.

Table 4. Anisotropy models

Anisotropy model	Type	v^P [km/s]	v^S [km/s]	Data	Sample/Model identification	Reference
Model I	TI	6.11	3.46	VSP	Model A	Jahns et al. (1996, table 1)
Model II	TI	5.57	3.33	VSP	Depth: 7.9-8.2 km	Rabbel et al. (2004, table 1)
Model III	TI	5.82	3.38	Sonic logs	Model B	Jahns et al. (1996, table 1)
Model IV	ORT	6.27	3.55	Lab	Model C	Jahns et al. (1996, table 1)

TI – transverse isotropy, ORT – orthorhombic anisotropy, v^P, v^S are average P and S velocities.

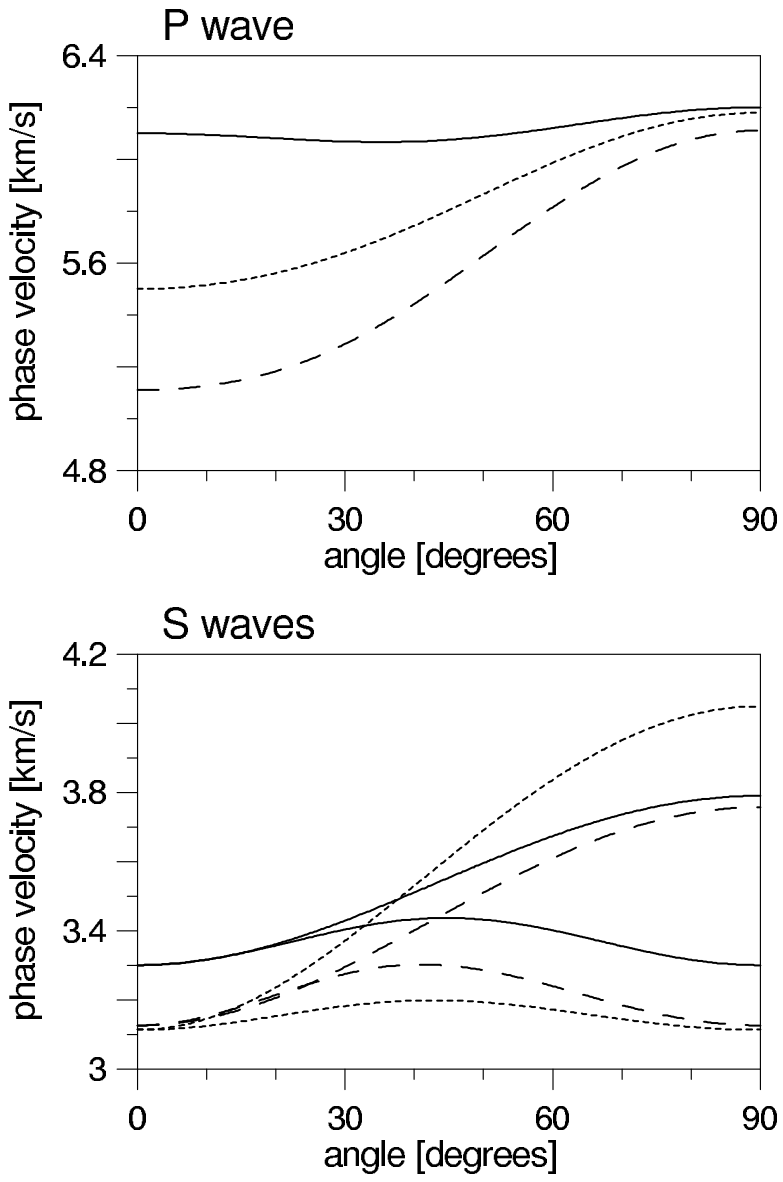

Figure 9. Directional variations of P- and S-wave velocities for three transversely isotropic models: Model I (solid line), Model II (dashed line), and Model III (dotted line). For the elastic parameters of the models, see Tab. 5. The angle defines the deviation between the slowness vector of the wave and the symmetry axis.

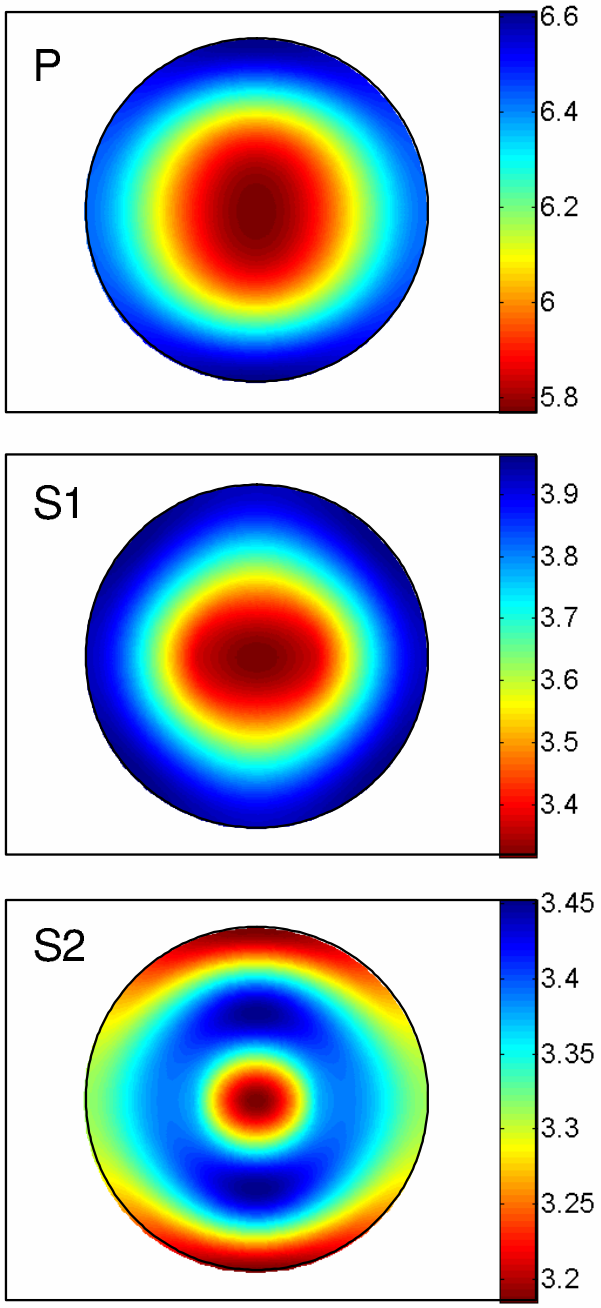

Figure 10. Directional variations of P- and S-wave velocities for Model IV displaying orthorhombic anisotropy. Velocities are in km/s. Equal-area projection is used. For the elastic parameters of the model, see Tab. 5.

Table 5. Anisotropy strength and density-normalized elastic parameters

Anisotropy model	a^P [%]	$a^{SV/S1}$ [%]	$a^{SH/S2}$ [%]	A_{11}	A_{22}	A_{33}	A_{44}	A_{55}	A_{66}	A_{12}	A_{13}	A_{23}
Model I	2.2	4.0	13.8	38.44	38.44	37.21	10.89	10.89	14.36	10.16	14.20	14.20
Model II	17.9	5.5	18.3	37.35	37.35	26.10	9.77	9.77	14.11	9.12	9.15	9.15
Model III	11.6	2.7	26.1	38.18	38.18	30.25	9.69	9.69	16.39	11.40	13.43	13.43
Model IV	13.6	17.8	8.1	41.27	43.73	33.28	10.14	10.98	15.41	11.09	14.00	14.14

a^P, $a^{SV/S1}$, $a^{SH/S2}$ denote the anisotropy strength for *P*, *SV* and *SH* waves in the case of TI anisotropy and the anisotropy strength for *P*, *S*1 and *S*2 waves in the case of ORT anisotropy. The anisotropy strength is defined as $a = 200\left(v^{MAX} - v^{MIN}\right)/\left(v^{MAX} + v^{MIN}\right)$, where v^{MAX} and v^{MIN} are the maximum and minimum phase velocities of the respective wave. Density-normalized elastic parameters A_{kl} are in km^2s^{-2}.

6.4. Inversion for optimum orientation of anisotropy from observed data

We adopted four alternative anisotropy models, described in the previous section, and inverted the moment tensors for the optimum orientation of anisotropy. The anisotropy orientation was sought over a sphere in a 5° grid of spherical angles. The misfit function was calculated using eq. (3) as the sum of determinants of source tensors of all earthquakes under study (see Vavryčuk 2004, eq. 10). Hence, we did not a priori assume any specific type of faulting, and the inversion was applicable to shear as well as non-shear earthquakes.

The results of the inversion are summarized in Tab. 6. Although the anisotropy models used in the inversion were fairly diverse, the found optimum orientations of the anisotropy axes are consistent for all of them. This points to the robustness of the inversion and plausibility of its results. Figure 11 shows the misfit functions for Models III and IV. Since Model III is transversely isotropic, the inversion yields only the orientation of the symmetry axis. Model IV is orthorhombic, and the inversion yields the orientations of all three anisotropy axes. The misfit function is normalized so that it equals 1 for an isotropic medium. For some orientations of anisotropy, the misfit function is even higher than for an isotropic medium. The optimum orientation of anisotropy yields the misfit of 0.81 for Model III and 0.77 for Model IV. Hence orthorhombic anisotropy fits the data slightly better than transverse isotropy. Nevertheless, the value of 0.77 of the misfit is still high and

points either to discrepancies between the used anisotropy model and the true anisotropy in the focal area, or to the fact that the non-DC components are significantly affected by random or systematic errors due to limitations of data or erroneous modeling of the structure in the moment tensor inversion.

Table 6. Inversion for anisotropy orientation

Model	Type	Axis 1 (azimuth/plunge)	Axis 2 (azimuth/plunge)	Axis 3 (azimuth/plunge)	Misfit
Model I	TI	65°/10°	---	---	0.85
Model II	TI	65°/5°	---	---	0.79
Model III	TI	70°/5°	---	---	0.81
Model IV	ORT	65°/5°	160°/50°	330°/40°	0.77

The misfit is normalized so that it equals 1 for an isotropic medium.

7. Non-DC components of the source tensors

The retrieved orientation of anisotropy can be used to estimate source tensors (2) from moment tensors (1). The source tensors should be, in principle, free of anisotropy effects and should contain only information on the geometry of faulting. Similarly as for moment tensors, we can decompose the source tensors into the DC and non-DC components and evaluate their percentages. Figure 12 shows a comparison of histograms of the ISO components for moment and source tensors calculated for Model IV. While the distribution of the ISO components is very broad for the moment tensors, it is remarkably narrow for the source tensors. The mean absolute value of the ISO is 13.5% for the moment tensors (see Tab. 7), but only 5.3% for the source tensors. Also the histograms of the CLVD for the moment and source tensors calculated for Model IV show visible differences (Fig. 13). While the CLVD distribution for the moment tensors is clearly asymmetric, the CLVD distribution for the source tensors is more symmetric. The mean value is shifted from -5.7% for moment tensors to 4.4% for source tensors (see Tab. 7). Hence, while compressive

components slightly prevail over tensile components in the moment tensors, we observe the opposite tendency in the source tensors.

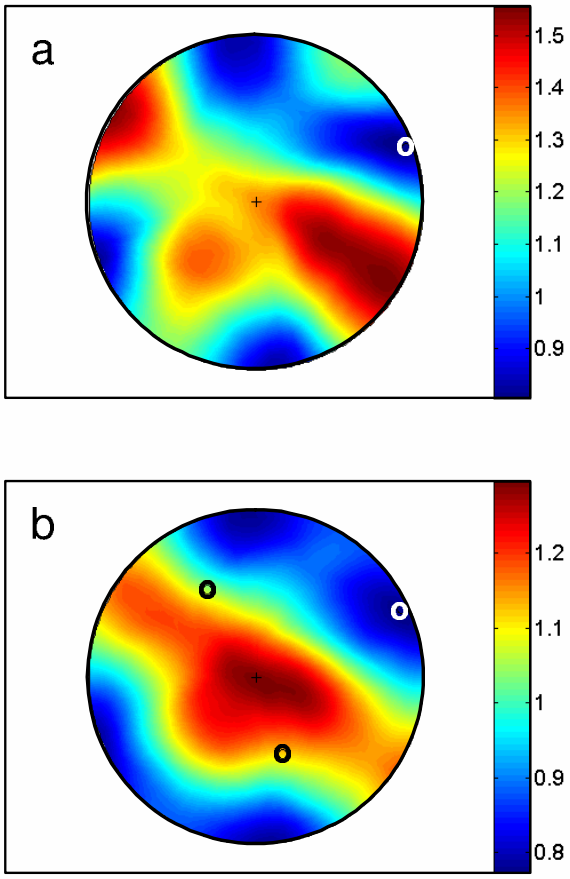

Figure 11. Inversion for the orientation of Model III (a) and Model IV (b). The misfit function is normalized so that it equals one for isotropic medium. For Model IV, the misfit function is displayed for anisotropy axis a_3 (vertical axis in the coordinate system of ORT).

8. Discussion

Although the quality and extent of the moment tensor dataset did not allow us to invert for a complete elasticity tensor but only for the orientation of anisotropy axes of transverse isotropy, or of orthorhombic anisotropy, the results are very encouraging. Although we applied four very different anisotropy models to mimic anisotropy in the focal area, the inferred optimum orientation of anisotropy axes is very consistent. The symmetry planes of the TI models and one of the symmetry planes of the ORT model are nearly vertical with a

strike of N335-340°E. This strike coincides well with the strike of 330° typical for many major lithological units and faults (Hirschmann 1996) and with the azimuth of 335-340° of the maximum horizontal compressive stress in the region. It also coincides with the orientation of the TI model inferred from P waves measured during a moving source profiling experiment (Rabbel et al. 2004, Okaya et al. 2004). Since the ORT model is close to TI, the orientation of the other two axes of the ORT model is more uncertain and less accurately determined. Rabbel et al. (2004, Fig. 12) predicted that their orientation depends on depth and propose three alternative orientations for the depth intervals: 0-4 km, 4-8 km, and an average model for 0-8 km (see Tab. 8). By comparing our results with these models (see Fig. 14), we obtain the best fit for the average model (0-8 km). In this case all three anisotropy axes coincide almost perfectly with mutual deviations of 18°, 12° and 14°. A worse fit is obtained if our results are compared with the anisotropy model at the 4-8 km depth. Here, both models predict an almost identical symmetry plane, but the two anisotropy axes in this plane deviate from one another by about 40°.

It is also worth mentioning that the non-DC components behave in a more reasonable way if corrected for anisotropy. The ISO percentages were significantly reduced using the anisotropy correction and the mean of the CLVD percentages moved from a negative to a positive value. However, the scatter of the CLVD values remained almost unchanged. This might point to discrepancies between true anisotropy in the focal area and the anisotropy models used in the inversion. It can also indicate that some of the events were generated on irregular or non-planar fractures. Another possibility is that the CLVD components are more vulnerable to errors in the moment tensor inversion than the ISO components.

Since the mean values of the ISO and CLVD components for all events under study are very small, we can conclude that tensile faulting is not a predominant type of faulting for the studied events. If it is present in some of the mechanisms, it must be rather minor. It turns out that the studied events do not reflect any stress perturbations at the focal area which could considerably affect the background stress field. Consequently, the pore pressure of the injected fluid did not achieve the minimum compressive stress for the majority of the active fractures, and the injected fluid triggered only shear events. This is in agreement with the model of fluid-injection-induced seismicity proposed by Baisch & Harjes (2003).

Table 7. Non-DC components of the 37 moment and source tensors

Model	Type	ISO^{MEAN} [%]	$CLVD^{MEAN}$ [%]	DC^{MEAN} [%]	$\|ISO\|^{MEAN}$ [%]	$\|CLVD\|^{MEAN}$ }%]	ΔISO [%]	ΔCLVD [%]
Moment tensors								
---	---	1,51	-5,70	60,38	13,48	26,14	---	---
Source tensors								
Model I	TI	0,11	0,70	68,97	5,54	25,49	-1,40	6,40
Model II	TI	2,29	3,42	68,19	6,20	25,61	0,78	9,12
Model III	TI	0,36	3,80	69,32	5,34	25,35	-1,15	9,50
Model IV	ORT	1,28	4,38	69,40	5,26	25,33	-0,23	10,08

ISO^{MEAN}, $CLVD^{MEAN}$ and DC^{MEAN} are mean values of percentages ISO, CLVD and DC, $|ISO|^{MEAN}$, $|CLVD|^{MEAN}$ and $|DC|^{MEAN}$ are mean values of absolute percentages |ISO|, |CLVD| and |DC| for the whole dataset of 37 events. ΔISO is the difference between the values of ISO^{MEAN} for source tensors and moment tensors. ΔCLVD is the difference between the values of $CLVD^{MEAN}$ for source tensors and moment tensors.

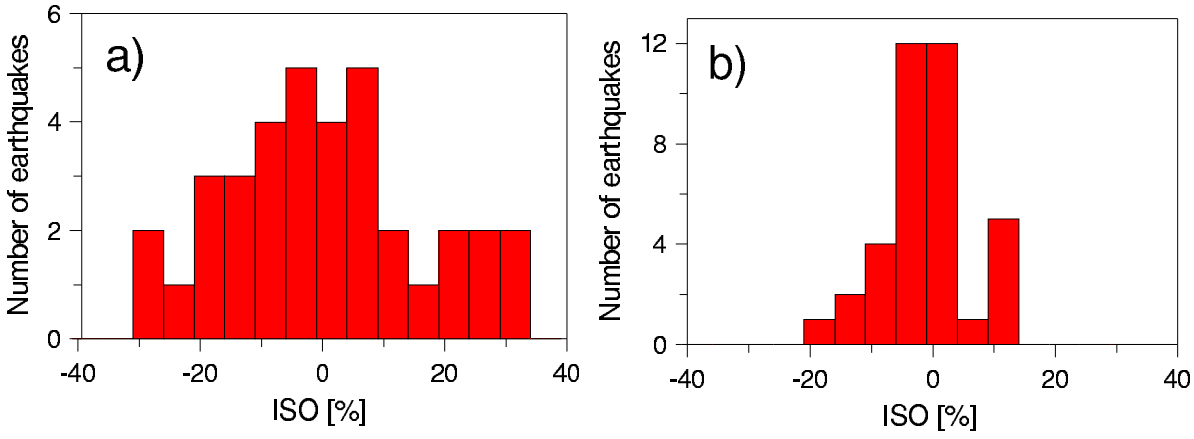

Figure 12. Histograms of the percentages of the ISO components calculated from the moment tensors (a) and from the source tensors (b). The source tensors are computed under the assumption of the anisotropic focal area defined by Model IV and oriented by the angles in Tab. 6.

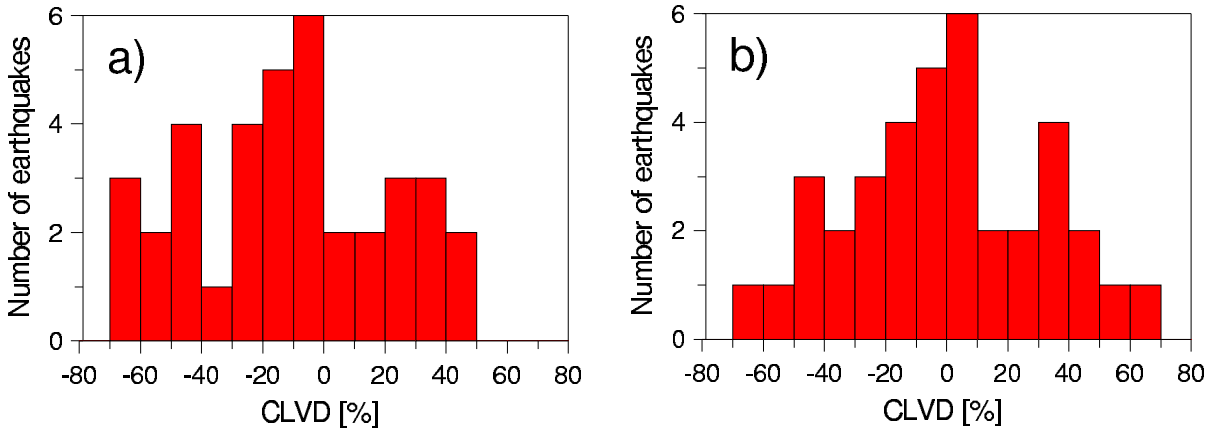

Figure 13. Histograms of the percentages of the CLVD components calculated from the moment tensors (a) and from the source tensors (b). The source tensors are computed under the assumption of the anisotropic focal area defined by Model IV and oriented by the angles in Tab. 6.

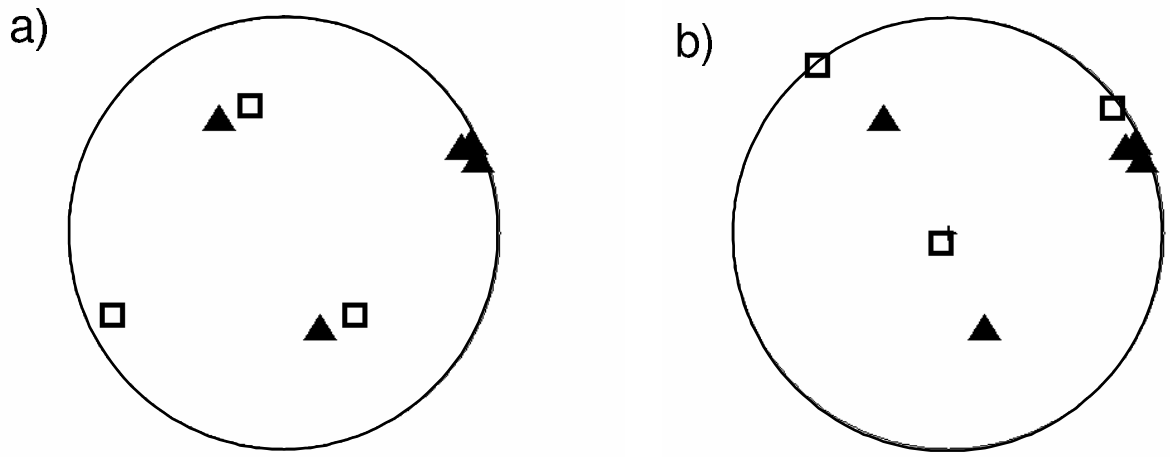

Figure 14. A comparison of retrieved orientations of anisotropy axes of Models I-IV (full triangles) with the orientations of anisotropy published by other authors (open squares). (a) Model inferred for the depth range of 0-8 km (Rabbel et al 2004), (b) model inferred for the depth range of 4-8 km (Rabbel et al. 2004). For values of the anisotropy orientations, see Tab. 8.

Table 8. Orientations of anisotropy at the KTB site.

Reference	Depth range	Axis 1 (azimuth/plunge)	Axis 2 (azimuth/plunge)	Axis 3 (azimuth/plunge)
This paper	5 – 6 km	65º/5º	160º/50º	330º/40º
Rabbel *et al* (2004, Fig. 12)	0 – 8 km	244º/13º	139º/48º	345º/39º
Rabbel *et al* (2004, Fig. 12)	0 – 4 km	268º/40º	155º/25º	42º/40º
Rabbel *et al* (2004, Fig. 12)	4 – 8 km	53º/5º	214º/85º	322º/2º

The azimuth is measured clockwise from North; the plunge is measured downwards from the horizontal direction.

9. Conclusions

- The fault plane solutions of the 37 selected events with the most reliable moment tensors show preferred strike-slip mechanisms with small normal or reverse components. The predominant azimuth of P and T axes is in the range of N140º-160ºE and of N50º-70ºE, respectively.
- The optimum principal stress directions inferred from focal mechanisms are (azimuth/plunge): $\sigma_1 = 335°/15°$, $\sigma_2 = 110°/70°$, $\sigma_3 = 240°/15°$, and the shape ratio is 0.55. The errors in the plunge and azimuth are about 10º. The resolved stress is consistent with the results obtained by Brudy et al. (1997).
- The retrieved moment tensors contain significant non-DC components. The DC is on average 60% and the non-DC is 40%. The non-DC components contain both the ISO and CLVD components. The mean value of ISO is 1.5%, the mean value of CLVD is -5.7%.
- The non-DC components probably have three major origins: random numerical errors produced by the moment tensor inversion due to noise and the limitations of input data, systematic errors produced by erroneous modeling of the medium when calculating the Green functions, and anisotropy in the focal area.

- The optimum orientation of the symmetry plane of TI inferred from non-DC components of the moment tensors is nearly vertical with a strike of N335-340°E. This strike coincides well with the strike of 330° typical for many major lithological units and faults and with the orientation of the TI model inferred from other seismic experiments (Rabbel et al. 2004, Okaya et al. 2004).
- After removing the anisotropy effects in the non-DC components, the distribution of the ISO is significantly narrowed. The mean value of the corrected ISO is close to zero and that of the corrected CLVD is shifted from a negative to a positive value. Specifically, assuming ORT anisotropy in the focal area, the mean CLVD changes owing to the anisotropy correction form -5.7% to 4.4%.
- Since the mean values of the corrected ISO and CLVD components are very small, we conclude that shear faulting is a predominant type of faulting in the studied dataset and pore pressure of the injected fluid was not high enough to open existing fractures. This confirms the model of fluid-injection-induced seismicity proposed by Baisch & Harjes (2003).

Acknowledgements

We thank Prof. Wolfgang Rabbel for providing us with details of the anisotropy models at the KTB site and Anthony Lomax for providing us with his program SeisGram2K used for data picking. The work was supported by the Grant Agency of the Academy of Sciences of the Czech Republic, Grants No. A3012309 and IAA300120502, by the Consortium Project SW3D "Seismic waves in complex 3-D structures", and by the EU Consortium Project IMAGES "Induced microseismics applications from global earthquake studies", contract No. MTKI-CT-2004-517242. A part of the work was done while the first author was a visiting researcher at the Schlumberger Cambridge Research, Cambridge, U.K.

References

Babuška, V. & Cara, M., 1991. *Seismic Anisotropy in the Earth*, Kluwer Academic Publishers, London.

Baisch, S., Bohnhoff, M., Ceranna L., Tu Y.& Harjes H.-P., 2002. Probing the crust to 9 km depth: Fluid injection experiments and induced seismicity at the KTB superdeep drilling hole, Germany, *Bull. Seism. Soc. Am.*, **92**, 2369-2380.

Baisch, S. & Harjes, H.-P., 2003. A model for fluid-injection-induced seismiciy at the KTB, Germany, *Geophys. J. Int.*, **152**, 160-170.

Berckhemer, H., Rauen, A., Winter, H., Kern, H. Kontny, A., Lienert, M., Nover, G., Pohl, J., Popp, T., Schult, A., Zinke, J. & Soffel, H.C., 1997. Petrophysical properties of the 9-km-deep crustal section at KTB, *J. Geophys. Res.*, **102**, 18.337-18.361.

Bohnhoff, M., Baisch, S. & Harjes, H.-P., 2004. Fault mechanisms of induced seismicity at the superdeep Germaan Conthinental Deep Dribling Program(KTB) borehole and their relation to fault structure and stress field, *J. Geophys. Res.*, **109**, B02309, doi: 10.1029/2003JB002528.

Brudy, M., Zoback, M. D., Fuchs, K., Rummel, F. & Baumgärtner, J., 1997. Estimation of the complete stress tensor to 8 km depth in the KTB scientific drill holes: Implications for crustal strength, *J. Geophys. Res.*, **102**, No. B8, 18.453-18.475.

Emmerman, R. & Lauterjung, J., 1997.The German Continental Deep Drilling Program KTB: Overview and major results, *J. Geophys. Res.*, **102**, 18.179-18.201.

Frohlich, C., 1994. Earthquakes with non-double-couple mechanisms. *Science*, **264**, 804-809.

Gephart, J. W., 1990. Stress and the direction of the slip on fault planes, *Tectonics*, **9**, 845-858.

Gephart, J. W. & Forsyth, D. W., 1984. An improved method for determining the regional stress tensor using earthquake focal mechanism data: Application to the San Fernando earthquake sequence, *J. Geophys. Res.*, **89**, No. B11, 9305-9320.

Hirschmann, G., 1996. KTB – The structure of a Variscan terrane boundary: Seismic investigation-drilling-models, *Tectonophysics*, **264**, 327-339.

Jahns, E., Rabbel, W. & Siegesmund, S., 1996. Quantified seismic anisotropy at different scales: a case study from the KTB crustal segment, *J. Geol. Wiss.*, **24**, 729-740.

Jahns, E., Siegesmund, S., Chlupáč, T., 1994. In situ seismic velocities versus laboratory measurements: an example fro the KTB, Scientific Drilling, 4, 215-226.

Jechumtálová, Z. & Šílený, J., 2005. Amplitude ratios for complete moment tensor retrieval, *Geophys. Res. Lett.*, **32**, art. No. L22303.

Jost, M.L. & Hermann, R. B., 1989. A student's guide to and review of moment tensors, *Seismol. Res. Lett.*, **60**, 37-57.

Julian , B. R., Miller, A. D. & Foulger, G. R., 1997. Non-double-couple earthquake mechanisms at the Hengill-Grensdalur volcanic complex, southwest Iceland, *Geophys. Res. Lett.*, **24**, 743-746.

Julian, B. R., Miller, A. D. & Foulger, G. R., 1998. Non-double-couple earthquakes 1: Theory, *Reviews Geophys.*, **36**, 525-549.

Kawasaki, I. & Tanimoto, T., 1981. Radiation patterns of body waves due to the seismic dislocation occurring in an anisotropic source medium, *Bull. Seismol. Soc. Am.*, **71**, 37-50.

Klíma, K., 1973. The computation of the elastic constants of an anisotropic medium from body waves, *Stud. Geophys. Geod.*, **17**, 115-122.

Lund, B. & Slunga, R., 1999 Stress tensor inversion using detailed microearthquake information and stability constraints: Application to Ölfus in southwest Iceland, *J. Geophys. Res.*, **104**, No. B7, 14947-14964.

Michael, A. J., 1987. Use of focal mechanisms to determine stress: A control study, *J. Geophys. Res.*, **92**, No. B1, 357-368.

Miller, A. D., Foulger, G. R. & Julian, B. R., 1998. Non-double-couple earthquakes 2: Observations, *Reviews Geophys.*, **36**, 551-568.

Müller, B., Zoback, M. L., Fuchs, K., Mastin, L., Gregersen, S., Pavoni, N., Stephansson, O. & Ljunggren, C., 1992. Regional patterns of tectonic stress in Europe, *J. Geophys. Res.*, **97**, 11.783-11.803, 1992.

Okaya, D., Rabbel, W., Beilecke, T. & Hasenclever, J., 2004. P wave material anisotropy of tectono-metaorphic terrane: An active source seismic exoeriment at the KTB super-deep drill hole, southeast Germany, *Geophys. Res. Lett.*, **31**, L24620, doi: 10.1029/2004GL020855.

Plenefisch, T. & Bonjer, K.P., 1997. The stress field in the Rhine Graben area inferred from earthquake focal mechanisms and estimation of frictional parameters, *Tectonophysics*, **275**, 7-97.

Rabbel, W., 1994. Seismic anisotropy at the Continental Dep Drilling site (Germany), *Tectonophysics*, **232**, 329-341.

Rabbel, W., Beilecke, T., Bohlen, T., Fischer, D., Frank, A., Hasenclever, J., Borm, G., Kück, J., Bram, K., Druivenga, G., Lüschen, E., Gebrande, H., Pujol, J. & Smithson, S., 2004. Superdeep vertical seismic profiling at the KTB deep drill hole (Germany): Seismic close-up view of a major thrust zone down to 8.5 km depth, *J. Gophys. Res.*, **109**, B09309.

Rössler, D., Rümpker, G. & Krüger, F., 2004. Ambiguous moment tensors and radiation patterns in anisotropic media with applications to the modeling of earthquake mechanisms in W-Bohemia, *Stud. Geophys. Geod.*, **48**, 233-250.

Ross, A. G., Foulger, G. R. & Julian, B. R., 1996. Non-double-couple earthquake mechanisms at the Geysers geothermal area, California, *Geophys. Res. Lett.*, **23**, 877-880.

Shimizu, H., Matsuwo, N. & Ohmi, S., 1988. A non-double-couple seismic source: Tensile-shear crack formation in the Unzen Volcanic Region, *Seismol. Res. Lett.*, **59**, No. 5, 1988.

Sipkin, S. A., 1986. Interpretation of non-double-couple earthquake mechanisms derived from moment tensor inversion, *J. Geophys. Res.*, **91**, No. B1, 531-547.

Šílený, J. & Vavryčuk, V., 2000. Approximate retrieval of the point source in anisotropic media: numerical modelling by indirect parametrization of the source, *Geophys. J. Int.*, **143**, 700-708, doi:10.1046/j.1365-246X.2000.00256.x.

Šílený, J. & Vavryčuk, V., 2002. Can unbiased source be retrieved from anisotropic waveforms by using an isotropic model of the medium?, *Tectonophysics*, **356**, 125-138. doi:10.1016/S0040-1951(02)00380-3.

Snoke, J. A., 2003. FOCMEC: Focal mechanism determinations, in *International Handbook of Earthquake and Engineering Seismology*, edited by W. H. K. Lee et al., Chap. 85.12, Academic, San Diego, California.

Vavryčuk, V., 2001. Inversion for parameters of tensile earthquakes, *J. Geophys. Res.*, **106**, No. B8, 16.339-16.355.

Vavryčuk, V., 2002. Non-double-couple earthquakes of January 1997 in West Bohemia, Czech Republic: Evidence of tensile faulting, *Geophys. J. Int.*, **149**, 364-373, doi:10.1046/j.1365-246X.2002.01654.x.

Vavryčuk, V., 2004. Inversion for anisotropy from non-double-couple components of moment tensors, *J. Geophys. Res.*, **109**, B07306, doi:10.1029/2003JB002926.

Vavryčuk, V., 2005. Focal mechanisms in anisotropic media, *Geophys. J. Int.*, **161**, 334-346, doi: 10.1111/j.1365-246X.2005.02585.x.

Vavryčuk, V., 2006a. Spatially dependent seismic anisotropy in the Tonga subduction zone: a possible contributor to the complexity of deep earthquakes, *Phys. Earth Planet. Inter.*, **155**, 63-72, doi:10.1016/j.pepi.2005.10.005.

Vavryčuk, V., 2006b. Focal mechanisms produced by shear faulting in weakly transversely isotropic crustal rocks, *Geophysics*, in print.

Wagner, G.A., *et al.*, 1997. Post-Variscan and thermal and tectonic evolution of the KTB site and its surroundings, *J. Geophys. Res.*, 102, 18.221-18.232.